ENGINEERING

Conformable ultrasound breast patch for deep tissue scanning and imaging

Wenya Du[1]†, Lin Zhang[1]†, Emma Suh[1,2]†, Dabin Lin[3]†, Colin Marcus[1,4], Lara Ozkan[1,4], Avani Ahuja[1,2], Sara Fernandez[1,5], Ikra Iftekhar Shuvo[1], David Sadat[1], Weiguo Liu[3], Fei Li[6], Anantha P. Chandrakasan[4], Tolga Ozmen[7], Canan Dagdeviren[1]*

Ultrasound is widely used for tissue imaging such as breast cancer diagnosis; however, fundamental challenges limit its integration with wearable technologies, namely, imaging over large-area curvilinear organs. We introduced a wearable, conformable ultrasound breast patch (cUSBr-Patch) that enables standardized and reproducible image acquisition over the entire breast with less reliance on operator training and applied transducer compression. A nature-inspired honeycomb-shaped patch combined with a phased array is guided by an easy-to-operate tracker that provides for large-area, deep scanning, and multiangle breast imaging capability. The in vitro studies and clinical trials reveal that the array using a piezoelectric crystal [Yb/Bi-Pb($In_{1/2}Nb_{1/2}$)O_3-Pb($Mg_{1/3}Nb_{2/3}$)O_3-$PbTiO_3$] (Yb/Bi-PIN-PMN-PT) exhibits a sufficient contrast resolution (~3 dB) and axial/lateral resolutions of 0.25/1.0 mm at 30 mm depth, allowing the observation of small cysts (~0.3 cm) in the breast. This research develops a first-of-its-kind ultrasound technology for breast tissue scanning and imaging that offers a noninvasive method for tracking real-time dynamic changes of soft tissue.

INTRODUCTION

Piezoelectric-based conformable electronics focusing on healthcare monitoring and biomedical applications have been intensively studied, ranging from on-body vital sign decoding to mechanical energy harvesting (*1*–*6*). To achieve insights and decoding into the deep tissue, piezoelectric-based ultrasound transducer technology has attracted substantial attention because of its advantages over computed tomography, a more costly and less accessible method that uses ionizing radiation, and magnetic resonance imaging (*7*, *8*). Although ultrasound bypasses radiation concerns, this technology faces fundamental challenges, limiting its ubiquitous integration with wearable technologies (*9*, *10*). In particular, it is not feasible for current ultrasound transducers to conform to curved body surfaces (*11*). Within the past 5 years, piezoelectric-based conformable ultrasound electronics have been intensively investigated for use in cardiac functions monitoring (*12*), hemodynamic imaging (*13*, *14*), blood flow monitoring (*15*), bladder volume observation (*16*), muscle activation monitoring (*17*), transdermal drug delivery (*18*), and imaging of many other internal organs (*19*, *20*). To optimize design outcomes, researchers seek to strike a balance between mechanical deformation, electrode stretchability, biocompatible adhesion, imaging quality, and performance stability (*12*, *19*). Although these wearable and flexible piezoelectric ultrasound devices have been proposed in recent years, some research pursuits remain untapped in the wearable ultrasound field, such as (i) the incorporation of state-of-the-art piezoelectric materials with ultrasound technologies and (ii) the realization of standardized, repeatable scanning over the large-area curvilinear soft tissues without applied transducer compression to allow accurate image reconstruction.

Piezoelectric materials play a critical role in the performance of ultrasound transducers. In previous studies, most conformable ultrasound transducers still used commercial lead zirconate titanate (PZT) ceramics (*12*–*19*). In pursuit of enhanced material properties, single crystals with morphotropic phase boundary (MPB) compositions, i.e., Pb($Mg_{1/3}Nb_{2/3}$)O_3-$PbTiO_3$ (PMN-PT), have been extensively investigated due to their high electromechanical coupling factors (k_{33} > 85%) and piezoelectric coefficients (d_{33} = 1200 to 2500 pC/N) (*21*). These values are far superior to those of commercial piezoelectric ceramics, such as PZT(d_{33} < 600 pC/N, k_{33} < 75%), making those materials promising candidates for ultrasonic transducers, actuators, and energy-harvesting devices (*22*, *23*). It has been demonstrated in bulky transducers with single elements or phased arrays that PMN-PT single crystal–based transducers exhibited enhanced acoustic performance compared to PZT-based transducers, including larger bandwidth, shorter pulse length, and higher axial and lateral resolution (*23*–*25*). However, the Curie temperature T_c (~150°C) and rhombohedral-to-tetragonal phase transition temperature $T_{r\text{-}t}$ (70° to 90°C) are quite low for PMN-PT solid solutions, which restricts their temperature usage range (*21*, *26*). Thus, searching for alternative relaxor-PT systems with (i) high T_c and $T_{r\text{-}t}$, and (ii) high d_{33} are highly desired. In recent years, researchers have begun to shift their focus on crystals doped with rare-earth elements to combat this trade-off and achieve both high $T_{r\text{-}t}$/T_c and d_{33} (*27*–*29*). For example, Sm^{3+}-doped PMN-PT crystals exhibited ultrahigh d_{33} (4100 pC/N) and dielectric constant (ε_r = 12,000) (*27*), and Nd^{3+}-doped Pb($In_{1/2}Nb_{1/2}$)O_3 (PIN)–PMN-PT also showed outstanding d_{33} (3240 pC/N) and ε_r (9246) (*29*). However, both of them had lower $T_{r\text{-}t}$ (~91°C). Therefore, it is

[1]Media Lab, Massachusetts Institute of Technology, Cambridge, MA 02139, USA. [2]Department of Mechanical Engineering, Massachusetts Institute of Technology, Cambridge, MA 02139, USA. [3]School of Opto-electronical Engineering, Xi'an Technological University, Xi'an 710021, China. [4]Department of Electrical Engineering and Computer Science, Massachusetts Institute of Technology, Cambridge, MA 02139, USA. [5]Department of Materials Science and Engineering, Massachusetts Institute of Technology, Cambridge, MA 02142, USA. [6]Electronic Materials Research Laboratory, School of Electronic Science and Engineering, Xi'an Jiaotong University, Xi'an 710049, China. [7]Division of Surgical Oncology, Massachusetts General Hospital, Harvard Medical School, Boston, MA 02114, USA.
*Corresponding author. Email: canand@media.mit.edu
†These authors contributed equally to this work.

imperative that an investigation be performed to assess the piezoelectric properties of the new ternary system with other doping elements to balance both criteria.

While harnessing novel materials in pursuit of more effective ultrasound technologies is crucial, imaging biological regions introduces some mechanical challenges. In the large-area, deep tissue imaging aspect, the human breast presents a particular challenge, as its geometry and deformability are highly variable not only between subjects but also at different times and ages within a given subject (see note S1). Thus, ultrasound plays a very important role in the diagnosis and treatment of breast cancer because it can be used to extract meaningful images from dissimilar breast tissue presentations (*30*, *31*). In current ultrasound breast imaging technologies, although the handheld ultrasonography (HHUS) and automated breast ultrasound (ABUS) are preferred methods (table S1), there are still technical gaps to overcome for ultrasound to become a reliable option for breast screening such as the following: (i) HHUS relies heavily on the expertise and training of the technician to manually scan the whole breast by applying a strong compression, and (ii) ABUS can scan the whole breast at once but still experiences poor skin contact due to the use of a liquid medium between the tissue and stationary, bulky machines in a hospital setting. Overcoming these gaps could not only help doctors reliably assess breast imaging but also provide a cost-effective, accessible, and user-friendly approach for early assessments of breast anomalies.

In summary, it is highly desirable—both from a transducer performance (i.e., superior material properties) and a breast imaging (i.e., repeatability of the array position, no applied compression, etc.) perspective—that a conformable patch exhibits enhanced acoustic properties and reliable imaging capability and achieve a full image of the typical four quadrants of the breast with easy operation (see note S1). In this work, we propose a conformable ultrasound breast patch (cUSBr-Patch) consisting of a one-dimensional (1D) phased array and an easily operable nature-inspired patch design (Fig. 1, A to C), which offers large-area, deep tissue scanning and multi-angle, repeatable breast imaging while avoiding the drawbacks of conventional ultrasound imaging technologies. The research flow (fig. S1) aims to show the novelty and structure of this work. We synthesized a Yb/Bi-doped PIN-PMN-PT single crystal with superior properties (d_{33} = 2800 pC/N, ε_r = 7000, k_{33} = 0.93) with a suitable phased transition temperature ($T_{r\text{-}t}$ > 105°C) compared to PZT and PIN-PMN-PT. We then fabricated a 1D phased array transducer consisting of 64 elements with an operational frequency of 7.0 MHz. The 1D array exhibits promising acoustic performance with (i) a maximum imaging depth of 80 mm, (ii) a contrast sensitivity of 3 dB, (iii) axial/lateral resolutions of 0.25/1.0 mm at 30 mm depth, and (iv) a larger field of view than the commercial handheld linear probe at depths of approximately 30 mm or deeper, indicating a potential reliable capability to detect early-stage breast tumors (see note S1). Beyond this, comprehensive in vitro experimental studies establish that the cUSBr-Patch can provide accurate and reproducible imaging on different phantoms. With the design of a scanning trace (Fig. 1, D and E) to physically guide transducer positioning alongside 360° rotation capabilities at each position (Fig. 1, F to I) integrated into a nature-inspired honeycomb patch, the 1D array can fully cover the entire breast surface and obtain a multiangle image reconstruction from different views (movie S1), thus overcoming fundamental issues that characterize present ultrasound technologies for whole-breast or large-area screening, namely, imaging artifacts because of poor positioning or lack of contact. This work pioneers a first-of-its-kind on-body ultrasound technology for breast tissue imaging and screening and serves as a novel noninvasive method to monitor the dynamic changes of breast tissue.

RESULTS

Conformable ultrasound breast patch design

The design objective was to develop a wearable interface between the 1D array and breast tissue that allows for consistent placement and orientation of the array in the sections of the breast (Fig. 1A). The nature-inspired honeycomb patch design is primarily composed of three components (Fig. 1B): (i) a soft fabric bra to serve as a familiar intermediary layer, (ii) a honeycomb patch as the outside layer to provide structure and guidance for the 1D array, and (iii) the tracker attached to the ultrasound array for handling and rotation of the array at a given location. The rectangular magnets (LOVIMAG) and circular magnets (Linlinzz) are used to adhere the patch onto the bra and hold the tracker on the patch openings, respectively (see Materials and Methods for details).

The fabric bra (Barely Zero by NEIWAI) is seamless, which gives full coverage to a wide range of breast sizes (A to DD). Rectangular magnets (Fig. 1B) were strategically placed and secured in optimal positions so that the outside patch could securely attach to the bra in the correct orientation. This also allowed for the cable of the 1D array to have full range of motion when gliding between the magnets. We cut circular holes that align with the openings of the patch into the bra so that the array could be in direct contact with the skin (Fig. 1J). Because of the symmetrical design of the patch, the bra can be turned inside out so that the ultrasound procedure can be applied to the other breast. The nature-inspired patch consists of a honeycomb pattern with open spaces for the tracker to move through as it traverses a specified path (Fig. 1D) to allow for a maximal field of view. The patch was designed with the consideration of four main criteria: (i) ease of use, (ii) range of motion (360° rotation at a given position with a repeatable array localization), (iii) sustainable manufacturing, and (iv) user comfort. Current ultrasound devices lack the accessibility for anyone and operation convenience (see note S1), whereas the honeycomb patch provides an intimate interface to supplement the reliable performance of the ultrasound array. The nature-inspired honeycomb design was created in Autodesk Fusion 360. Honeycomb structures have been preferred in medical devices because they minimize the amount of material used in manufacturing, maximize flexibility, easily cover large areas of the skin, and provide structural stability, allowing for the conformability of the patch and the customization of array scanning (*32*, *33*). The 2 mm–thick patch is layered with a white thermoplastic polyurethane (TPU) layer and a gray color polylactic acid (PLA) layer, achieving a dual effect of conformability to the body and strong rigidity in the structure of the patch (Fig. 1E). There are six openings in the patch where the tracker can be rotated up to 360° (Fig. 1, G to I). Furthermore, the tracker is able to traverse through a path of up to 15 hexagonal sections (Fig. 1D), which makes the scanning straightforward for localizing the lesion beyond the typical four-quadrant designation (Fig. 1, C to E, and movie S1). The combined field of views from each opening

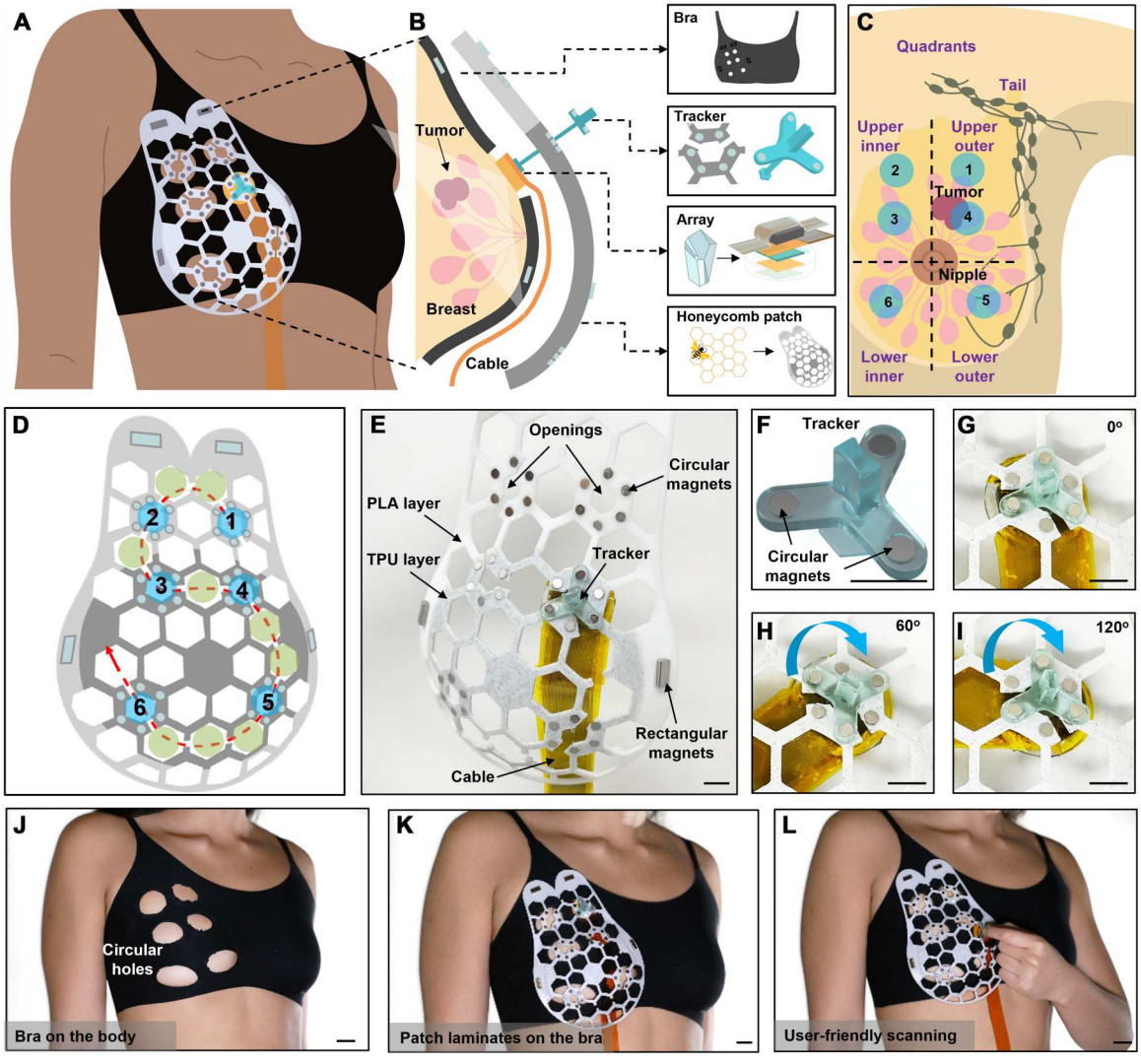

Fig. 1. The overview of the design of the cUSBr-Patch. (**A**) Schematic of a cUSBr-Patch on the body. (**B**) Exploded view of the cUSBr-Patch to illustrate its four main components: a soft fabric bra to serve as a familiar intermediary layer, a honeycomb patch as the outside layer to provide structure and guidance of the 1D array, the tracker to hold and rotate the 1D array, and the single crystal–based 1D phased array. (**C**) Schematic of breast quadrants and the positions of circular regions that align with the patch openings and circular holes in the bra. (**D**) Schematic of the honeycomb patch with six main openings (blue areas). The red dashed line indicates the specific trace for the 1D array scanning. The light green areas indicate additional nine hexagonal sections for imaging. (**E**) Photo of the honeycomb patch with the array and tracker. (**F**) Photo of the tracker. (**G** and **I**) Photos of the tracker rotating clockwise from 0° to 120°, demonstrating its capability for a 360° rotation. (**J**) Photo of the fabric bra with circular holes on a healthy human subject. Circular holes are designed to specifically serve as openings for the array to have intimate integration with skin and align with patch openings. (**K**) Photo of the patch attaching on the bra without mechanical delamination. (**L**) Photo of an easy-to-operate scanning. Scale bars, 1 cm (E) to (I) and 2 cm (J) to (L).

sufficiently covers the relevant areas of the breast, allowing for a comprehensive set of overlapping ultrasound images.

The tracker is attached to the 1D array to provide ease of slotting into predetermined imaging positions and is able to move freely around the patch (Fig. 1, D and F, and movie S1; see Materials and Methods for details). The circular magnets were bonded to their positions within the patch after being put into each of the circular press-fit notches (Fig. 1E). Because of the placement of the circular magnets embedded in the patch, there are six main positions for the tracker that are each 60° apart (Fig. 1, G to I). Openings in the patch are patterned around the corresponding circular holes in the bra for array placement so that the round magnets can be notched in. Three equidistant prongs extend out from the center of the tracker with circular pockets extruded from each prong to fit a circular magnet. The combination of the array and the tracker allows the tracker to continuously be sandwiched between the skin and the patch (Fig. 1K). A handle on the top of the tracker allows the user to grip and operate it (Fig. 1L).

Piezoelectric performance of Yb/Bi-PIN-PMN-PT crystal

In this work, we focused on the ternary PIN-PMN-PT system for achieving high phase transition temperatures (T_c and $T_{r\text{-}t}$) and enhanced d_{33}. For a multicomponent ferroelectric system, the linear combination rule is used to predict the MPBs in ternary systems

(*34*). This rule checks that the MPBs of ternary systems are in the linear area between the MPBs of binary systems (see note S2). The studied composition of PIN-PMN-PT was based on the experimental data from the polycrystalline region located near the predicted MPB region, as shown in Fig. 2A (marked by a red dot). A phase diagram of the co-doped PIN-PMN-PT system is plotted in contrast with PMN-PT and PIN-PMN-PT systems, as shown in fig. S2. Because the tolerance factor of the PIN (0.964) end member is smaller than that of the PMN (0.989), it is clear that the PIN-PMN-PT system is expected to have a wide temperature utilization range and advanced piezoelectric properties. As a result, the T_c and $T_{r\text{-}t}$ of PIN-PMN-PT crystals are 160° to 180°C and 90° to 110°C, respectively, which are higher than the T_c (130° to 150°C) and $T_{r\text{-}t}$ (70° to 90°C) of PMN-PT crystals. In addition, it has been reported that the performance of PMN-PT single crystals decreases obviously- with decreasing sample thickness (increasing working frequency) (*35*). Crystals with finer domains exhibit improved piezoelectric and dielectric properties under the high-frequency range of the pulse field (*36*). The PIN-PMN-PT crystals have a smaller domain size than PMN-PT crystals, making them more appropriate for high-frequency (>10 MHz) ultrasonic transducers. In addition, the aim of element doping is to have good thermal stability and high piezoelectric performance concurrently. The motivation for selecting Yb as the doping element is that (i) the ionic radius of Yb^{3+} (0.87 Å) is very close to the ionic radius of Sm^{3+} (0.96 Å) because the Sm^{3+}-doped crystal showed record-high piezoelectric properties (*27*) and (ii) a quantitative analysis of a Yb doped for PIN-PMN-PT piezoelectric crystal has yet to be reported (*37*, *38*).

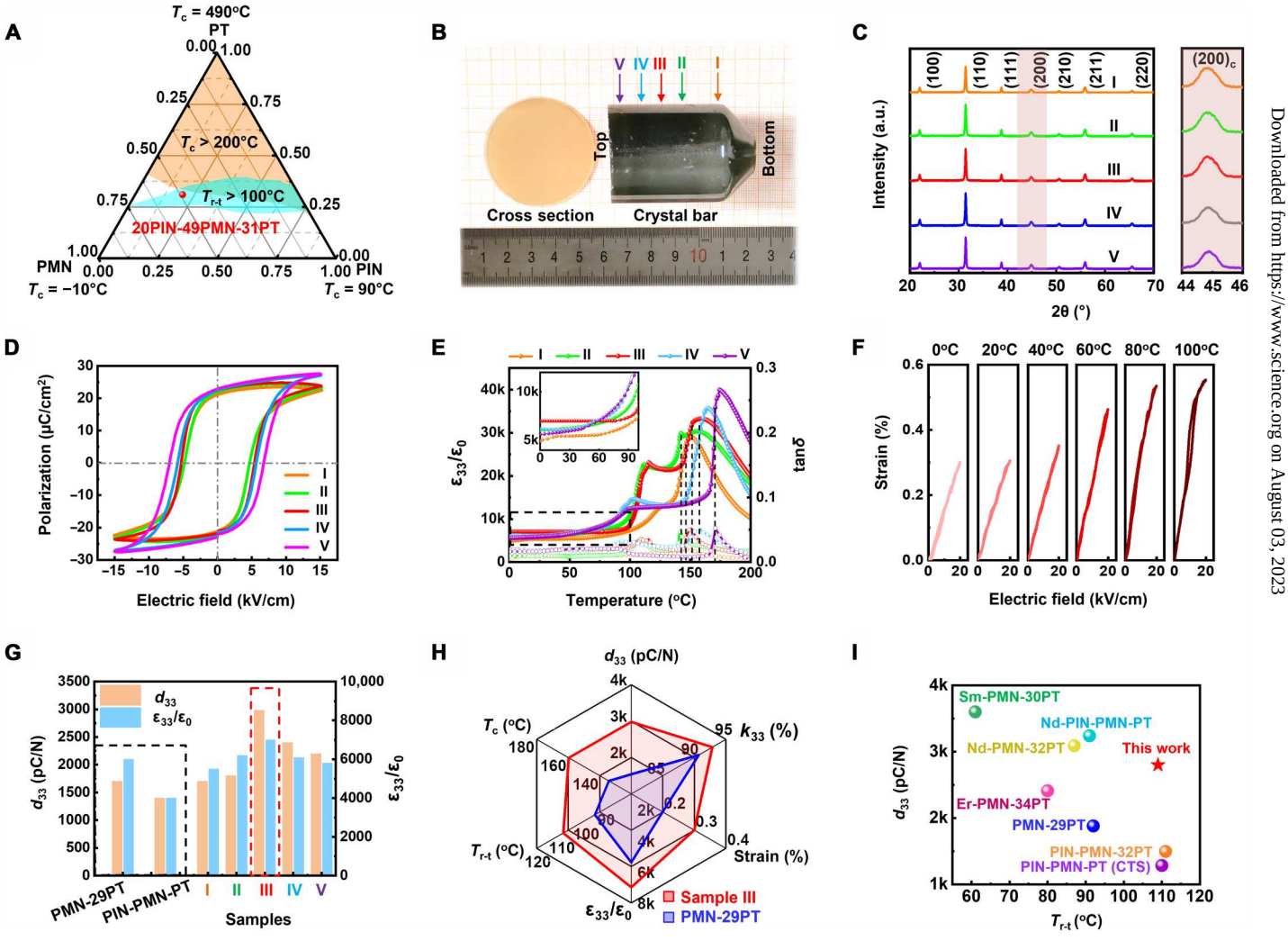

Fig. 2. The structure and properties of the Yb/Bi-PIN-PMN-PT single crystal. (**A**) Phase diagram of the PIN-PMN-PT single crystal. (**B**) Photograph of the as-grown Yb/Bi-PIN-PMN-PT single-crystal boule and polished cross section. Five samples, I to V, were diced from different positions of the rod for routine characterization. (**C**) XRD patterns of samples I to V. Inset: Enlarged region around 2θ = 45°. a.u., arbitrary units. (**D**) Hysteresis loops of all samples. (**E**) Temperature-dependent dielectric permittivity of specimens of all samples. Inset: Enlarged region around 0° to 100°C. (**F**) The electric field–induced strain behavior of sample III at selected temperatures: 0°, 20°, 40°, 60°, 80°, and 100°C. (**G**) The piezoelectric coefficient d_{33} and dielectric permittivity $\varepsilon_{33}/\varepsilon_0$ properties of samples I to V and PMN-PT and PIN-PMN-PT crystals. (**H**) Radar chart comparing the overall performance of Yb/Bi-PIN-PMN-PT (sample III) with published results of the PMN-29PT single crystal. (**I**) d_{33} versus $T_{r\text{-}t}$ for the Yb/Bi-PIN-PMN-PT crystals, with a comparison to other reported rare-earth–doped PMN-PT and PIN-PMN-PT crystals. The detailed comparison with reported literature and references is listed in table S4.

The motivation for selecting Bi as the co-doped element is that Bi can prevent the decrease of T_c (*39*). The as-grown crystal boule and polished cross section of Yb/Bi co-doped PIN-PMN-PT crystals are shown in Fig. 2B. As labeled, five samples were diced from different positions of the rod for routine structural characterization to facilitate subsequent performance testing. The x-ray diffraction (XRD) pattern of all samples in Fig. 2C indicates good structural consistency and a pure perovskite structure. The symmetric peaks around 45° in the enlarged region imply that all samples have a rhombohedral phase. The energy-dispersive x-ray spectroscopy element mapping (fig. S3) also indicates homogeneous specimen microstructures. Figure 2D shows the polarization–electric field hysteresis loops for crystals. The remnant polarization P_r was found to increase from sample I to sample V due to the increase of the number of possible polar directions as the composition approaches the MPB region. Meanwhile, E_c was found to increase monotonically from sample I to sample V, indicating that domain switching becomes more difficult due to the increased tetragonality. Thus, the structure and properties of a co-doped piezoelectric single crystal, namely, Yb/Bi-PIN-PMN-PT, were successfully quantified (Fig. 2), which has not been reported in the literature.

In piezoelectric transducer applications, higher E_c would allow transducers to be driven in a higher electrical field and higher $T_{r\text{-}t}$ for a broader temperature usage range (*40*). When the operating temperature or electric field exceeds $T_{r\text{-}t}$ or E_c, the transducer becomes depolarized. As a result, piezoelectric performance should be stable throughout a wide range of temperatures and electric fields to enable the creation and operation of piezoelectric devices. Figure 2E and fig. S4 display the temperature dependence of the dielectric properties of five samples. The dielectric constant increases gradually before the $T_{r\text{-}t}$, and the $T_{r\text{-}t}$ value of all samples is higher than 95°C, which shows improved dielectric temperature stability compared to other reported crystals. In addition, Fig. 2F shows the temperature-dependent unipolar strain curves (*S*-*E*) in which the slope increases with increasing temperature from 0° to 80°C, and a phase transition is observed at 100°C. The location dependences of d_{33} and ε_r for the Yb/Bi-PIN-PMN-PT ternary system are given in Fig. 2G. For sample III, the d_{33} and $\varepsilon_{33}/\varepsilon_0$ values were found to be on the order of ~2100 pC/N and ~6500, respectively, which is higher than that of PMN-PT and undoped PIN-PMN-PT crystals. In addition, the XRD pattern of sample III in fig. S5 indicates consistent structural form from 0° to 100°C. The standard pigment-dispersing factor cards of PMN-32PT and PMN-38PT single crystals are also added to show the rhombohedral phase and tetragonal phase, respectively. The symmetric peaks around 45° in the enlarged region indicate a rhombohedral phase below the $T_{r\text{-}t}$ temperature. Other parameters similarly support sample III′s viability in fig. S6.

As a result, sample III was chosen for further investigation. The measurement of five specimens from sample III with different dicing orientations is shown in table S2 and fig. S7 (see note S3), and the full matrix electromechanical properties of this crystal are listed in table S3. Figure 2H plots the comparison of six crucial ferroelectric properties between Yb/Bi-PIN-PMN-PT and the commercially used PMN-29PT single crystals by the radar chart. This graph makes it quite evident that Yb/Bi-PIN-PMN-PT single crystals have significant benefits over PMN-29PT and solve the trade-off of enhancing piezoelectric performance at the expense of the phase-transition temperature. In addition, table S4 lists the general features of various single crystals, including rare-earth–doped single crystals for comparison, and Fig. 2H illustrates the d_{33} versus $T_{r\text{-}t}$ values compared with recently reported crystals (*27*–*29*, *41*–*44*). The Yb/Bi-PIN-PMN-PT single crystal shows promising piezoelectricity, larger E_c, and higher $T_{r\text{-}t}$. In summary, the crystal synthesis follows our design and expectation that the adding dopant elements can increase piezoelectricity, while introducing PIN composition can raise the coercive field and phase transition temperature. The promising piezoelectric and dielectric properties, high $T_{r\text{-}t}$, and large E_c make the Yb/Bi-PIN-PMN-PT single crystal suitable for high-voltage and high-frequency acoustic applications such as high-performance medical transducer arrays. In the following work, specimens diced from sample III of Yb/Bi-PIN-PMN-PT single crystals were used for the ultrasound transducer fabrication.

Performance of 1D ultrasound arrays

The 1D phased array was designed on a standard transducer three-port network (*23*), which includes the active piezoelectric element, backing layer, and two matching layers, depicting the geometry of the 1D phased array with its main components (fig. S8). According to the literature, the recommended transducer frequency for imaging breast tumors ranges from 5 to 12 MHz (table S1). For breast scanning and imaging purposes, a 1D phased array with 64 elements and a working frequency of 7.0 MHz and a wavelength (λ) of 220 μm were chosen to strike a balance between the demands for depth and spatial resolution. The pitch value of 125 μm (0.56λ) was slightly above the phased array requirement of 0.5λ, to achieve wide-angle imaging and reduce grating lobes (*45*–*47*). The element width is 95 μm, and the kerf is 30 μm, determined by the thickness and vibration of the dicing blade (DISCO Corporation, Japan). The element length is chosen to be 8 mm (64 times the pitch) to achieve a minimally dispersed acoustic beam within the intended imaging depth. The cross-sectional view reveals that the epoxy solution under high-temperature pressure has firmly bonded all of the components, giving them a consistent thickness (fig. S8B; see Materials and Methods for details). After bonding with matching layers, backing layer, and the anisotropic conductive film (ACF) cable (fig. S9), the thickness of the entire device is still less than 3 mm. The frequency dependence of electric impedance and phase of single element are shown in Fig. 3A. The resonance and antiresonance frequencies are 5.9 and 8.1 MHz, respectively, resulting in a large effective electromechanical coupling coefficient (k_{eff} = 0.68). The array also showed a −6 dB bandwidth of 70% with the center frequency around 7.1 MHz (Fig 3B), which is slightly smaller than the simulation results (79%) by the Krimholtz-Leedom-Mattaei model due to the fabrication processing, flexible cable, or unmatched electric circuit (see note S4 and fig. S8F). In addition, the array′s electrical impedance and acoustic performances were measured to investigate the uniformity of array elements. The performance of all elements of the array is shown in Fig. 3C.

To enable real-time imaging, a data acquisition interface connected the array to a Vantage 256 system (Verasonics Inc.) (fig. S10; see Materials and Methods for details). The array was tested on two different phantoms to quantify their acoustic performance and imaging capacity before conducting human clinical trials (see Materials and Methods for details). First, a planar ultrasound phantom with wire and cylinder targets (model 040GSE, Computerized Imaging Reference Systems Inc.) was used to demonstrate the field of view and resolution (fig. S11 and movie S2). The 2D images

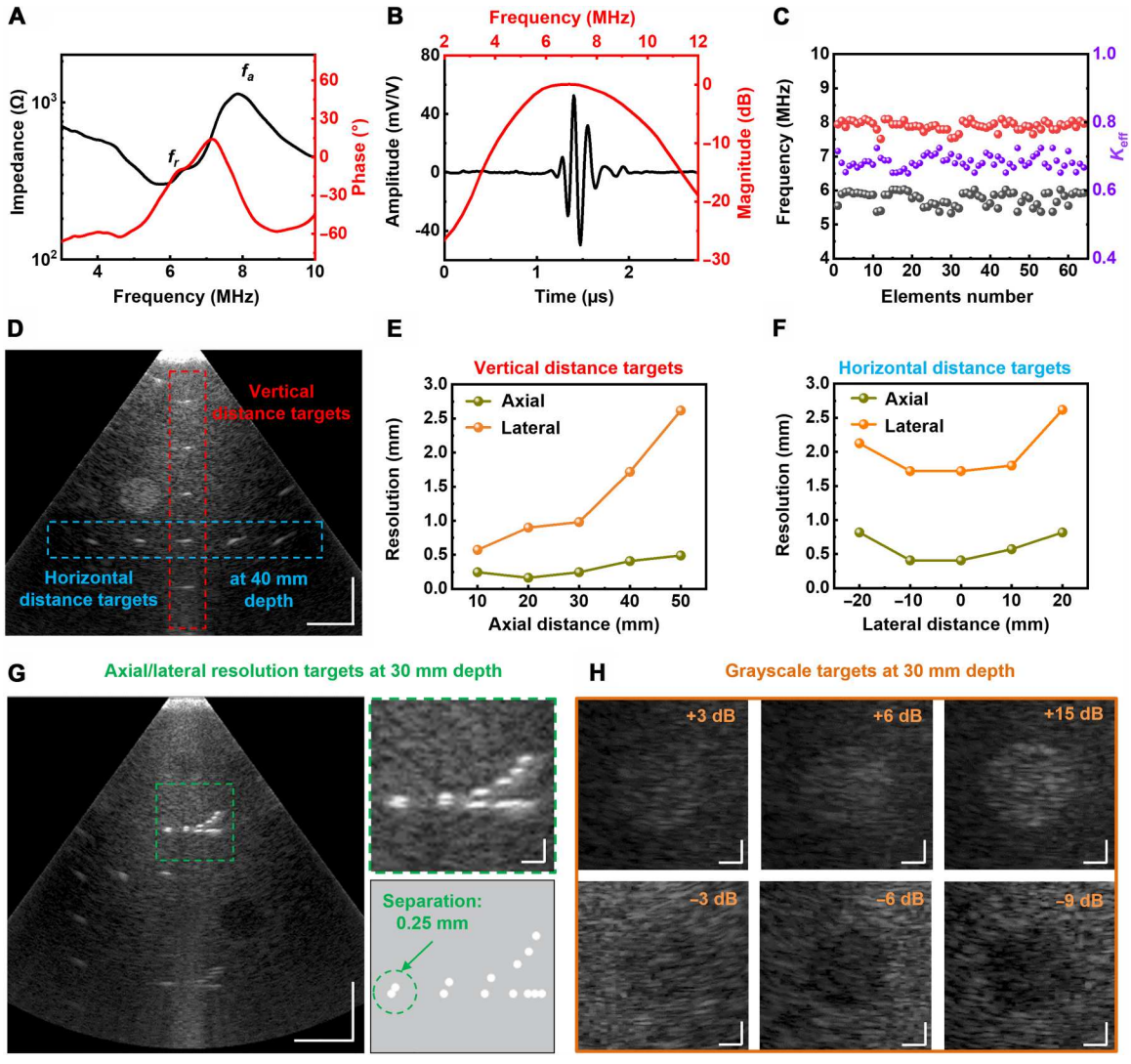

Fig. 3. The piezoelectric and acoustic performance of 1D phased array. (**A**) Electrical impedance spectrum of a single element of the phased array. (**B**) Measured waveform and frequency spectrum of the single element of the phased array. (**C**) Resonance frequency, antiresonance frequency, and electromechanical coupling coefficient of 64 elements of the phased array. (**D**) Ultrasound image of vertical distance targets (red dashed area) and horizontal distance targets (blue dashed area). (**E**) Lateral and axial resolutions of the 1D array at different depths. (**F**) Lateral and axial resolutions of the 1D array with different lateral distances from the central axis. (**G**) Ultrasound image of axial/lateral resolution targets at 30 mm. The zoomed-in view green dashed area in (G) and the schematic of the axial/lateral resolution targets indicate the separations between targets. (**H**) Ultrasound images of the grayscale group at 3 cm depth with hyperechoic targets (+3, +6, and +15 dB) and hypoechoic targets (−3, −6, and −9 dB). Scale bars, 1 cm (D) and (G) and 2 mm (green dashed area in (G) and (H).

on vertical and horizontal distance targets (Fig. 3D), axial and lateral resolution targets (Fig. 3G), and hyperechoic/hypoechoic targets (Fig. 3H) were obtained. The results demonstrate that the phased array has a maximum field of view of up to 100 mm width and an imaging depth of approximately 80 mm (fig. S11C). For the resolution targets at 30 mm depth, the array separated targets with gaps as small as 0.25 mm in the axial direction and 1.0 mm in the lateral direction, indicating a promising resolution for soft tissue imaging under skin around 30 mm (Fig. 3, E and F). In addition, hyperechoic/hypoechoic targets can be used to determine the minimum contrast sensitivity of the array. The images on different grayscale targets from +15 to −9 dB are at the depth of 30 mm as shown in Fig. 3H. The results indicate that the 1D array can clearly identify the lowest contrast targets with −3 and +3 dB in this phantom, which demonstrates the sufficient contrast sensitivity (~3 dB) of this 1D array (*12*, *45*). To further evaluate the imaging quality of the cUSBr-Patch on a curved surface, the oval phantom (model US-18, Kyoto Kagaku Co. Ltd.) was used (fig. S12). Six individual images were taken that depict a large sphere object, a tube object, a bean-shape object, a square pyramid object, a cylinder object, and a cubic object in different depths and locations both clearly and distinctly (movie S3). To investigate the thermal dissipation of the array, the temperature of the device was measured via a thermal camera (Teledyne FLIR LCC) over a period of 10 min while the device was being operated by a Vantage 256 system at a working voltage of 50 V. The array can keep a constant surface temperature

(23°C within 7% variation) under 50 V for 10 min due to its low working power and relatively thin structure (<3 mm) for heat dissipation (fig. S13). Both the phantom data and thermal test revealed that our phased array is suitable for clinical studies on human soft tissue (*48*).

In vivo study on breast tissue

A female subject with a history of breast anomalies was recruited (see Materials and Methods for details). We first imaged both breasts using the cUSBr-Patch with the Vantage 256 system and then cross-validated the results by an ML6-15 linear probe with the GE Logiq E10 system (fig. S14). Figure 4 (A and B) shows the patch on the left breast and the scan sequence from positions 1 to 6 along the designed trace in the patch (Fig. 1D and movie S4). Because of the reasonable maximum image depth and axial/lateral resolution, we can clearly observe various breast tissue from different positions (Fig. 4, C to H). At position 4, a cyst with a diameter of 1 cm can be detected, which appears as well circumscribed and hypoechoic due to the lower acoustic impedance than the surrounding tissues. To better define the lesion shape, the array at positions 1 to 4 was rotated by manipulation of the tracker from its initial 0° orientation to 60° and 120°, respectively (Fig. 4, I to L, and fig. S14). The cyst is identified as a roughly spherical shape via all three ultrasound images at various angles. The multiangle reconstructed images and video based on the rotation images are shown in Fig. 4 (M to O) and movie S5.

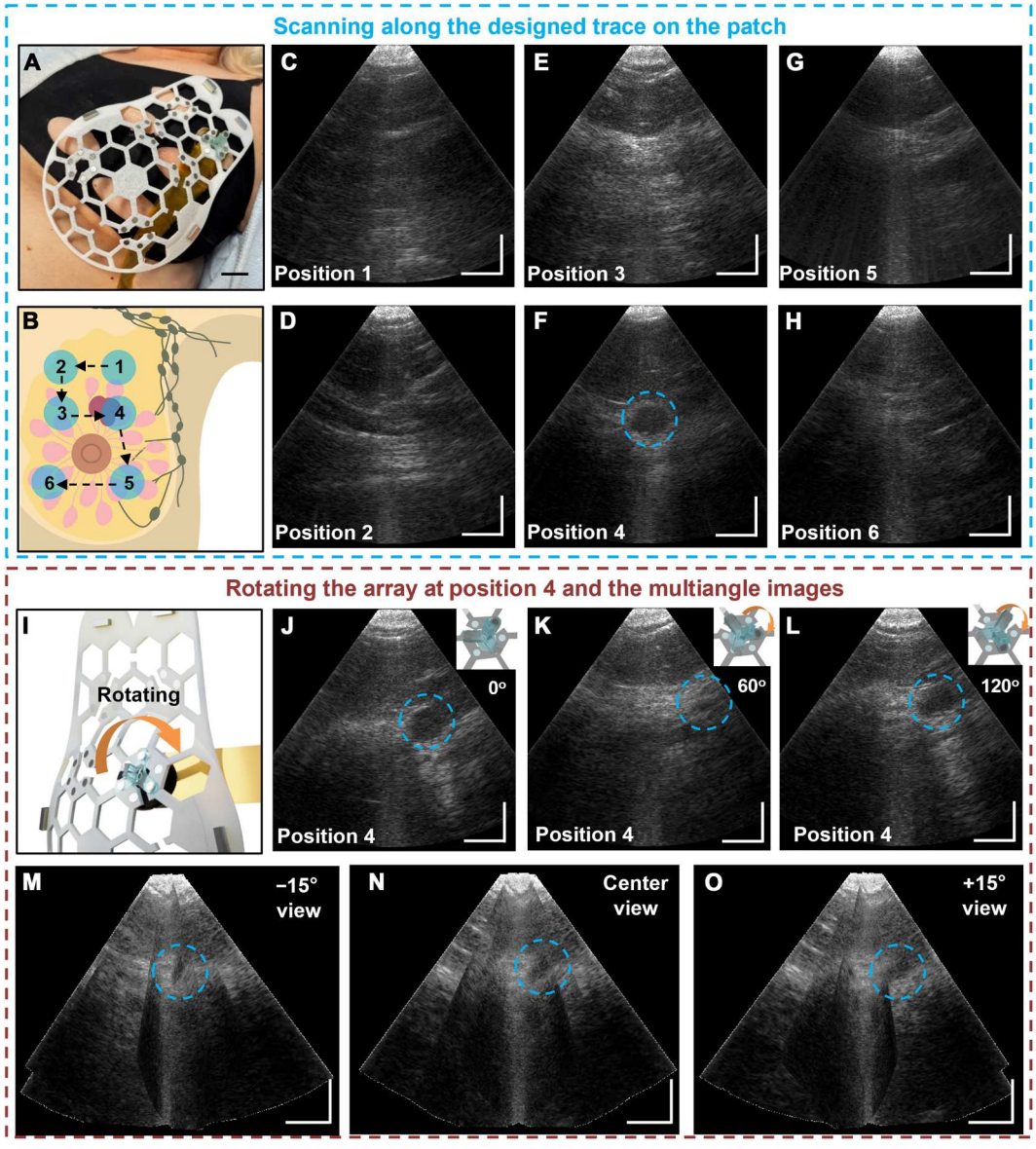

Fig. 4. The in vivo study on breast tissue. (**A**) Photo of the cUSBr-Patch on the left breast of a female subject. (**B**) Schematic of the scanning trace on the breast at six different positions of the honeycomb patch. (**C** to **H**) Ultrasound images at positions 1 to 6. (**I**) Schematic of the array rotation by the tracker. (**J** to **L**) Ultrasound images by the array when it is rotated clockwise at different angles (0°, 60°, and 120°) at position 4. (**M** to **O**) Multiangle image reconstruction at position 4 with different view angles (−15°, center view, and +15°). The blue dashed circle indicates the hypoechoic lesion. Scale bars, 2 cm (A) and 1 cm (C) to (H) and (J) to (O).

We also used the same scanning sequence to examine the right breast of the subject (fig. S15). A smaller cyst with a diameter of 0.3 cm was detected by the cUSBr-Patch in the right breast. After finishing the examination on both breasts, we then used the GE ML6-15 linear array commercial probe with the setting at the same frequency (7 MHz) to cross-validate the imaging results by the cUSBr-Patch. The ultrasound specialist checked the same region on both breasts and found a larger cyst (diameter of 1 cm) in the left breast and a smaller cyst (diameter of 0.3 cm) in the right breast (fig. S17), which indicates that our patch can precisely observe these lesions and has the potential reliable capability to detect early-stage breast tumors (see note S1). The cUSBr-Patch′s ability to identify abnormalities on the order of 0.1 cm is essential for achieving early breast cancer detection well before tumors reach 2 cm in size (*49*). In addition, when we compare the field of view, this 1D phased array with a narrower aperture (8 mm in lateral dimension) provides the same field of view (fan shape with the 50-mm field of view at 3-cm depth) as the GE ML6-15 (fig. S18). It also shows a great field of view at depths deeper than 30 mm. Although the phased array may not completely cover some shallow places close to the skin surface, this is still appropriate for deep lesions because the breast tumor has a very low probability near the skin and fat (within 10-mm depth) (*50*–*52*). Furthermore, before the cross-validation, we used the patch to check the imaging performance stability over time. The array can still detect the large cyst at position 4 with similar image quality after 30 min with 15 min intervals (fig. S19), indicating the repeatability of array positioning due to the honeycomb patch, a key capability to enable long-term monitoring. In summary, we attempted to address the enormous challenge of imaging on the breast, which has the largest curvature on the human skin, in comparison to very recent designs that rely on hydrogels for fixed adhesion of the single-ultrasound array (*19*) or the design based on a stretchable substrate with hundreds of elements for long-time imaging (*12*). Either using a substrate with a large number of elements to completely cover the breast or frequently attaching/peeling a small patch at various locations on the breast is not a desirable strategy. In addition, unlike heart, bladder, and other organ monitoring, breast imaging concentrates on the exact location of the cyst in the breast rather than requiring continuous imaging during a person′s activities. This is the reason that we proposed the first-of-its-kind on-body ultrasound technology that used the combination of a conformable patch with a rotated phased array, to combine the advantages of HHUS and ABUS, especially for breast application. The cUSBr-Patch uses a nature-inspired honeycomb design to hold the array in place such that the array can be easily rotated and moved to different positions to enable the observation of breast tissue in a more streamlined and standardized manner. The cUSBr-Patch additionally circumvents the need for a 3D scanner or complex beamforming algorithm by using a high-frequency phased array transducer with a fixed element pitch (*12*).

DISCUSSION

In this work, we introduced a first-of-its-kind ultrasound technology with a nature-inspired design, which offers noninvasive, large field-of-view, real-time, user-friendly, and continuous monitoring of curved breast tissue in a wearable form factor. This work follows a comprehensive system approach, from the synthesis and characterization of an advanced piezoelectric crystal, to array design and performance evaluation, to nature-inspired patch design, to a clinical demonstration with real-time imaging on the breast, and culminates in a brand-new device for noninvasive soft tissue scanning and imaging.

The 1D array′s integration with a nature-inspired patch, together with the superior electromechanical performance of the Yb/Bi PIN-PMN-PT crystal (d_{33} = 2800 pC/N, $\varepsilon_{33}/\varepsilon_0$ = 7000, T_c = 160°C, $T_{r\text{-}t}$ = 109°C, and E_c = 5.3 kV/cm), offers high-performance image production with (i) deep image depth (~80 mm), (ii) sufficient contrast sensitivity (~3 dB at 30 mm depth), (iii) desired axial/lateral resolution (0.25/1.0 mm), and (iv) a larger field of view for breast tissue imaging, which is cross-validated with a commercial ultrasound probe (Figs. 3 and 4). In addition, the nature-inspired honeycomb patch design provides several advancements including (i) the ability to traverse through a path of 15 imaged sections (Fig. 3D), which makes the scanning straightforward for localizing the lesion location outside of the typical four-quadrant designation; (ii) mechanical support and stability for the array, with a tracker to achieve images at different angles via rotation; (iii) the elimination of the requirement for an operator to constantly hold the device, which is especially critical for freeing up the operator′s hands during future home-based screening; and (iv) great repeatability positions, demonstrating reliable and comparable breast tissue screening for long-term monitoring. For use in practical applications, additional advantages prevail, such as reusability, ease of operation, and increased feasibility for at-home continuous monitoring of breast abnormalities from an earlier stage when lesion dimensions do not yet exceed 2 cm (see note S1). The cUSBr-Patch′s ability to discernibly image cysts with diameters around 0.3 cm makes it suitable for early breast cancer screening (fig. S16). For large-area imaging, the individual users can move the array to different positions along the honeycomb-shaped patch to obtain an all-encompassing representation, while the hospital can use more arrays simultaneously to achieve spatiotemporally accurate imagery by multiangle image reconstruction.

Future research will concentrate on a number of advancements, ranging from introducing a size-customizable patch with a polymer substrate, embedded with multiple 1D arrays to avoid random manual scanning, to intensive clinical trials with long-term imaging during the course of medical treatments or medication, to a portable system with back-end capabilities that enable daily self-screening. Thus, this could allow individualized ultrasonographic profile generation along with big data collection (e.g., tissue images and artificial intelligence–analyzed results) to send to medical practitioners for fast and objective assessments. Such systems may be developed to co-integrate with wireless communication for continuous clinical monitoring of a wide range of soft tissue conditions in which image variations, measured by the cUSBr-Patch, can be anticipated via either time-dependent alterations in progression in soft tissue anomaly or a response throughout medical therapy.

MATERIALS AND METHODS

Fabrication of the nature-inspired patch

The patch was printed with a 3D printer (Prusa i3 MK3S+) with two different layers of material: a white color TPU layer and a marble color PLA layer (Fig. 1E). The print started with a white TPU filament at 100% infill and was programmed to pause at a specific layer

of the patch. The TPU was then exchanged for marble (PLA and the printer continued until the part was completed). The connections between the different materials were strengthened with superglue in the areas of attachment that were not strong enough to provide adequate connection initially. The Linlinzz circular magnets were inserted in each of the circular notches, which were designed to be press-fit, and were also glued to reinforce their position within the patch. All magnets were oriented such that they had the same direction of polarity (Fig. 1E). The patch's cup shape was designed and tested to fit the breast of a pregnant participant who grew from a size B to D cup during pregnancy. Four rectangular magnets (LOVIMAG, 12 mm by 5 mm by 3 mm) were superglued to the outside of the patch on the ears of the tab that attach to the upper part of the bra and the sides of the cup so that the patch could adhere to the rectangular magnets embedded within the bra. The cup itself contains four circular magnets that attach to the tracker for placement of the array around the nipple. A nearly flat tab of the patch contains two more circular openings that allow further detection in the upper quadrant of the chest, extending toward the axilla (Fig. 1D). For the patch to cling to the rectangular magnets contained within the bra, four rectangular magnets were superglued to the exterior of the patch on the ears of the tab that attach to the top of the bra and the sides of the cup.

The tracker was printed at a 45° angle in a ELEGOO MARS 2 resin printer with acrylonitrile butadiene styrene–like photopolymer resin material (Fig. 1F). It was then cured for strength with a UV Cure Box machine so that the tracker was strong enough to withstand the torsion forces experienced during the carrying and rotating of the 1D array. The number of prongs was chosen to maintain planar stability while both minimizing the material needed for the tracker and reducing the manufacturing complexity. The circular magnets (Linlinzz, diameter: 2 mm, thickness: 1 mm) on the tracker align with the magnets on the patch because they have the same specific distance from the center and 600° apart. The press-fit magnets were again reinforced with superglue in the tracker, and the magnets were flipped in the correct orientation to align with the magnets in the patch. The magnets were aligned between the two cloth layers of the bra in the correct orientation to attract the patch's rectangular magnets. The rectangular magnets were placed in the bra such that the center part of the patch covered the nipple and the tab extended in the direction of the axilla. A supporting rectangular magnet was placed on the outside of the bra to secure each of the inner magnets in their proper position (Fig. 1E). The inner magnets were then secured by sewing the two layers of black thread through both of the bra's fabric layers around the rectangular magnets. All magnets were oriented such that they had the same direction of polarity. After each inner magnet was sewn in, the securing outer magnet was able to be removed. The circular outlines of the array were then marked and cut out of the bra, in alignment with the patch openings. To connect the tracker and array within the assembly, the tracker was magnetically attached and steadied on the outer surface of one of the openings of the patch. The stem protruded into the cup and the handle extended away from the cup. The end of the stem was then superglued to the center of the array.

Preparation of piezoelectric single crystals

The Yb and Bi co-doped PIN-PMN-PT single crystals were grown by a modified Bridgman method. First, $InNbO_4$ and $MgNb_2O_6$ precursor materials were fabricated at 1100° and 1200°C for 6 hours, respectively. The Pb_3O_4, $MgNb_2O_6$, $InNbO_4$, Yb_2O_3, Bi_2O_3, and TiO_2 powders were wet-mixed using zirconium ball milling with ethyl alcohol as a solvent for 24 hours. Then, the mixed powders were calcinated at 850°C for 2 hours and vibratory milled in the ethanol for 24 hours. The presynthesized ternary compound was loaded into a cylindrical Pt crucible with a single crystal seed at the bottom. The crucible was then placed into a three-zone vertical Bridgman furnace. The obtained crystal boule with a diameter of 40 mm and a length of about 50 mm (Fig. 2B).

Characterization of piezoelectric single crystals

The crystal structure of the samples was determined via XRD (Bruker D8). Energy-dispersive x-ray elemental maps of samples were measured by a field-emission scanning electron microscope (Zeiss Gemini SEM 500). For further electric measurement, a silver paste was fired on both sides of the samples at 600°C for 10 min to form the electrodes. The samples were poled in silicone oil at 25°C for 10 min using a DC electric field with a strength of 15 kV/cm. The piezoelectric coefficients were determined by a combination of the impedance method and a quasi-static d_{33} meter. In the resonance method, the resonance and antiresonance frequencies were measured using an HP4194A impedance analyzer. The unipolar strain induced by the external electric field was then measured using a linear differential transducer driven by a lock-in amplifier (Stanford Research Systems, model SR830) connected to a computer-controlled cooling-heating stage.

Fabrication of 1D phased array

The 1D phased array was fabricated and assembled at both the Center for Nanoscale Systems at Harvard University and the cleanroom facility (YellowBox) of the Media Lab at the Massachusetts Institute of Technology. Three steps were involved in the fabrication: (i) the creation of a 64-element 1D array, (ii) electrode deposition and patterning followed by cable bonding, and (iii) the creation of matching and backing layers. The traditional dice-and-fill method was used to fabricate the 1D phased array. To achieve 65 dicing lines on the sample, a dicing machine (DISCO, Tokyo, Japan, model DAD 321) with a 15-μm–thick synthetic diamond blade (DISCO, Tokyo, Japan, Z09-SD3000-Y1-60) was used. To increase the crystal footprint and minimize damage from blade vibration, our research laboratory generated the appropriate specifications for DISCO to custom manufacture the ultrathin dicing blade. The dicing pitch, kerf, and actual width of each element were 125, 30, and 95 μm, respectively. To avoid any mechanical harm on the elements, the dicing speed was fixed at 0.25 mm/s. The dicing depth was roughly 350 μm, which was greater than the final desired thickness to allow for further polishing. The epoxy (EPO-TEK 301, Epoxy Technology Inc., USA) was used to fill the kerf and eliminate the transverse vibration in the ceramic by vacuum degassing and was cured at 65°C for 2 hours. After lapping the top surface to expose ceramic elements, the conductive epoxy strip (E-Solder 3022, Von Roll USA Inc.) was added on both sides to connect the bottom electrode to the top surface (fig. S8). Last, the entire array was polished to the designed thickness and encapsulated by the epoxy again in a round mold.

The chromium (Cr, 10 nm) and gold (Au, 300 nm) were deposited on the upper surface of the array by electron beam (e-beam) evaporation (Denton e-beam deposition). A layer of photoresist

(AZ 5214-E IR, MicroChem Corp.) was spin coated onto the electrode at a speed of 3000 rpm for 60 s and then baked at 65°C for 10 min. Then, the array was ultraviolet exposed for 10 s under a mask aligner (MJB4, SÜSS MicroTec SE, Germany), developed for 60 s in a developer (MIF AZ 726, MicroChem Corp.), and then wet etched by Au and Cr etchant solution for 120 and 20 s, respectively. After stripping with acetone, isopropyl alcohol (IPA), and deionized water, the final electrode pattern on the top surface is completed, including 64 traces of electrodes and 2 wide traces on strips of E-Solder 3022 (fig. S8). Last, the chromium (Cr, 10 nm) and gold (Au, 300 nm) layers were deposited on the bottom surface of the array by e-beam evaporation again. The bottom electrode fully covered all elements and strips of E-solder 3022. The ACF cable was bonded to the array and the printed circuit board interface under a microscope. The bonding area was applied with strong pressure and cured in the oven at 65°C for 1 hour.

The final array was obtained by adding the matching layer and the backing layer. For the matching layer preparation, the zirconia oxide powder [5 μm, 99%; Chemical Abstracts Service (CAS) no.: 1314-23-4, Sigma-Aldrich Inc.] was selected as the filler and the epoxy (EPO-TEK 301, Epoxy Technology Inc. USA) was used as the matrix. The ZrO_2 powder and epoxy solution were first mixed with the ratio of 3:1 to obtain a homogeneous mixture, poured into the mold, centrifuged at 2000 rpm for 10 min, and then cured at 65°C for 2 hours in the oven. After polishing the first matching layer to the designed thickness, the epoxy solution was cast on the surface of the first matching layer and polished to achieve the second matching layer. For backing layer preparation, the tungsten (W) powder (APS 1 to 5 μm, 99.9%; CAS no.: 7440-33-7, Alfa Aesar) was selected as the filler, and the epoxy (EPO-TEK 301, Epoxy Technology Inc. USA) was used as the matrix. The W powder and epoxy solution were first mixed with a ratio of 4:1 to obtain a homogeneous mixture, which was poured into the mold, centrifuged at 2500 rpm for 10 min, and then cured at 65°C for 2 hours in the oven. The final backing layer was obtained by polishing the surface to the designed thickness. Last, the matching and backing layers were bonded onto the array by the epoxy solution. Firm pressure was applied to the bonding area, which was then cured in the oven at 65°C for 1 hour.

Characterization of 1D array

The electrical impedance of the diced elements and the fabricated array were measured in the air at room temperature using an impedance analyzer (Agilent E4991A, Agilent Technologies, Santa Clara, CA, USA). Two key parameters, resonance frequency (f_r) and antiresonance frequency (f_a), can be obtained from the impedance spectrum. The effective electromechanical coupling coefficient (k_{eff}) is calculated with the following formula

$$k_{\text{eff}} = \sqrt{\frac{f_a^2 - f_r^2}{f_a^2}} \tag{1}$$

For acoustic testing to obtain the bandwidth, a pulser/receiver (JSR Ultrasonics DPR 300) was used to individually excite single elements from the transducer with a voltage of 100 V and then received by the element itself. A large disk quartz was located in the water tank for reflection. The relative position between the array and the quartz was adjusted to achieve the strongest signal. The two-way echo response was captured by the element itself and displayed on an oscilloscope (PicoScope 5444B), while the frequency domain was calculated by fast Fourier transform (FFT). The center frequency f_c and −6 dB bandwidth (BW%) were calculated by

$$f_c = \frac{f_1 + f_2}{2} \tag{2}$$

$$\text{BW}\% = \frac{f_2 - f_1}{f_c} \times 100\% \tag{3}$$

where f_1 and f_2 are the frequency when the magnitude of the FFT of the echo is −6 dB, and f_1 is smaller than f_2.

Assembly and operation of the nature-inspired patch

The subject first wears the bra with the embedded magnets on the side of the breast. The patch, carrying the connected tracker and array, snaps onto the bra via the aligning rectangular magnets. The subject moves the array through the notched path of the patch and into the desired location along the breast by gripping the handle of the tracker. When the array is in the opening locations and contacts the skin, the ultrasound image can be obtained with the Vantage 256 system. In addition, the array can be rotated to various orientations and the flexible cable between the patch and the bra can slip between the magnets to achieve full 360° rotation. The array can be held in place without further manual support due to the magnetic connection between the tracker and the patch. The patch and its components can be removed by detaching the rectangular magnets sewn into the bra from the rectangular magnets attached to the patch. The bra can be turned inside out for evaluation of the other breast and the process can be completed. Following the imaging procedure, the subject can wear the bra with the embedded magnets alone. Despite the consistent design, the magnets alone are not strong enough to ensure consistency in the tilt of the array without manual support from the user. The stem protruding from the bottom center of the tracker is super glued onto the back of the ultrasound array, permanently fusing the two parts. The stem is 2.5 mm in diameter, thin enough to be maneuvered through the path of notches in the patch, which are 4 mm in width.

Acoustic imaging on phantoms

The multipurpose, multi-tissue ultrasound phantom (model 040GSE Computerized Imaging Reference Systems Inc.) was used for performance and quality assurance testing of the phased array (fig. S10). For this phantom, the gel was used to ensure the acoustic coupling (Aquasonic 100 Ultrasound Transmission Gel, Parker Laboratories Inc.). The US-18 fundamental ultrasound phantom (Kyoto Kagaku Co. Ltd.) with an oval shape and curved surface was used for the array imaging on different 3D objects (fig. S11).

Human clinical study

All procedures on the subject with breast anomaly history were conducted in accordance with the experimental protocol approved by the Committee on the Use of Humans as Experimental Subjects of the Massachusetts Institute of Technology (MIT) (COUHES, no. 2011000271). The participants completed the informed consent forms. Inclusion criteria were female gender, age 18 to 85 years, and body mass index between 17 and 40 kg/m^2. Subjects were excluded for having significant health problems (such as chronic or acute cardiovascular diseases and skin diseases) and physical and/

or behavioral health disabilities limiting the ability to follow directions and complete research-related activities. Subjects may have the following unhealthy breast or related problems (such as breast pain, breast tenderness, tumors, cysts, fibroadenomas, fat necrosis, sclerosing adenosis, generalized breast lumpiness, etc.). The clinical study was conducted at the MIT Center for Clinical and Translational Research (CCTR) (fig. S14). Imaging was performed using the Vantage 256 system with the cUSBr-Patch first and then verified by the clinical GE Logiq E10 (GE Healthcare, Waukesha, WI) with a linear probe (GE ML6-15). Scan 11-08 Ultrasound Gel (Parker Laboratories Inc.) was used for acoustic coupling. Two clinical research nurse coordinators of the MIT CCTR and one clinical applications specialist of the GE Healthcare were assisted in this study.

The subject at the age of 71 with a body mass index of 37, who has abnormal breast history, was recruited. The subject was asked to lay supine on an examination table and adjust her clothing to ultrasound scanning access to her breast. First, we scanned the breast using the phased array on the subject's left breast clockwise from the outer edge to the nipple and then located the lesion and scanned the breast. Second, the subject was asked to wear the designed bra and patch. Then, we scanned the left breast again at six different locations according to the patch design, then test the reliability and obtained multiangle images by rotation after the right breast scanning. To verify the imaging, after removing the bra and patch, the specialist used the GE ML6-15 probe on the subject's breast to scan again clockwise from the outer edge to the nipple and confirmed the lesions and their locations. Last, the ultrasound gel was cleaned from the subject's skin by a clean wiper.

Beam forming and image processing

Real-time imaging was performed using a standard focused beamforming method. Transmit delays were set up to scan across ±45° with 128 ray lines. The imaging depth was set to 60 mm with the transmit focus at 50 mm. The transmit excitation was a single cycle sine at 50 V, with center frequency set to 7.0 MHz. The imaging dynamic range was set to 60 dB. A triangular apodization was used, which provides high spatial resolution while reducing side lobes to −27 dB. Time-gain control was adjusted manually to increase with depth, attenuating strong signals close to the array while amplifying signals far from the array to provide a more uniform image brightness. The representative videos (movie S4) were screen recorded using Open Broadcaster Software. In post-processing, a Python script was used to crop the video to show just the ultrasound image and then the image dynamic range was rescaled as desired. Generally, the dynamic range was rescaled to 55 dB, because higher dynamic ranges begin to show the noise floor. The array imaging resolution was assessed using the 040GSE phantom, which includes wire targets split into axial and lateral groups (Fig. 3D). The image of each wire target was cropped, the dynamic range was converted to 6 dB, and the axial and lateral point spread function (PSF) dimensions were measured to produce Fig. 3 (E and F). For the multiangle image reconstruction, the video was cropped, and the dynamic range was rescaled as previously discussed. The images corresponding to 0°, 60°, and 120° rotations (Fig. 4, J to L) were then combined into a 3D image using Napari, a Python 3D rendering library. The multiangle image was rotated by ±15° to make the 3D nature of the image more apparent, as shown in Fig. 4 (M to O) and movie S5.

Supplementary Materials

This PDF file includes:
Notes S1 to S4
Figs. S1 to S19
Tables S1 to S4
Legends for movies S1 to S5
References

Other Supplementary Material for this manuscript includes the following:
Movies S1 to S5

REFERENCES AND NOTES

1. C. Dagdeviren, Z. Li, Z. L. Wang, Energy harvesting from the animal/human body for self-powered electronics. *Annu. Rev. Biomed. Eng.* **19**, 85–108 (2017).
2. C. Dagdeviren, Y. Su, P. Joe, R. Yona, Y. Liu, Y. S. Kim, Y. A. Huang, A. R. Damadoran, J. Xia, L. W. Martin, Y. Huang, J. A. Rogers, Conformable amplified lead zirconate titanate sensors with enhanced piezoelectric response for cutaneous pressure monitoring. *Nat. Commun.* **5**, 4496 (2014).
3. M. T. Chorsi, E. J. Curry, H. T. Chorsi, R. das, J. Baroody, P. K. Purohit, H. Ilies, T. D. Nguyen, Piezoelectric biomaterials for sensors and actuators. *Adv. Mater.* **31**, 1802084 (2019).
4. T. Sun, F. Tasnim, R. T. McIntosh, N. Amiri, D. Solav, M. T. Anbarani, D. Sadat, L. Zhang, Y. Gu, M. A. Karami, C. Dagdeviren, Decoding of facial strains via conformable piezoelectric interfaces. *Nat. Biomed. Eng.* **4**, 954–972 (2020).
5. C. Dagdeviren, F. Javid, P. Joe, T. von Erlach, T. Bensel, Z. Wei, S. Saxton, C. Cleveland, L. Booth, S. McDonnell, J. Collins, A. Hayward, R. Langer, G. Traverso, Flexible piezoelectric devices for gastrointestinal motility sensing. *Nat. Biomed. Eng.* **1**, 807–817 (2017).
6. S. V. Fernandez, F. Cai, S. Chen, E. Suh, J. Tiepelt, R. McIntosh, C. Marcus, D. Acosta, D. Mejorado, C. Dagdeviren, On-body piezoelectric energy harvesters through innovative designs and conformable structures. *ACS Biomater Sci. Eng.* **9**, 2070–2086 (2023).
7. R. Guo, G. Lu, B. Qin, B. Fei, Ultrasound imaging technologies for breast cancer detection and management: A review. *Ultrasound Med. Biol.* **44**, 37–70 (2018).
8. J. A. Jensen, Medical ultrasound imaging. *Prog. Biophys. Mol. Biol.* **93**, 153–165 (2007).
9. D. Ren, Y. Yin, C. Li, R. Chen, J. Shi, Recent advances in flexible ultrasonic transducers: From materials optimization to imaging applications. *Micromachines* **14**, 126 (2023).
10. M. Lin, H. Hu, S. Zhou, S. Xu, Soft wearable devices for deep-tissue sensing. *Nat. Rev. Mater.* **7**, 850–869 (2022).
11. H. Hu, X. Zhu, C. Wang, L. Zhang, X. Li, S. Lee, Z. Huang, R. Chen, Z. Chen, C. Wang, Y. Gu, Y. Chen, Y. Lei, T. Zhang, N. H. Kim, Y. Guo, Y. Teng, W. Zhou, Y. Li, A. Nomoto, S. Sternini, Q. Zhou, M. Pharr, F. Lanza di Scalea, S. Xu, Stretchable ultrasonic transducer arrays for three-dimensional imaging on complex surfaces. *Sci. Adv.* **4**, eaar3979 (2018).
12. H. Hu, H. Huang, M. Li, X. Gao, L. Yin, R. Qi, R. S. Wu, X. Chen, Y. Ma, K. Shi, C. Li, T. M. Maus, B. Huang, C. Lu, M. Lin, S. Zhou, Z. Lou, Y. Gu, Y. Chen, Y. Lei, X. Wang, R. Wang, W. Yue, X. Yang, Y. Bian, J. Mu, G. Park, S. Xiang, S. Cai, P. W. Corey, J. Wang, S. Xu, A wearable cardiac ultrasound imager. *Nature* **613**, 667–675 (2023).
13. C. Wang, X. Li, H. Hu, L. Zhang, Z. Huang, M. Lin, Z. Zhang, Z. Yin, B. Huang, H. Gong, S. Bhaskaran, Y. Gu, M. Makihata, Y. Guo, Y. Lei, Y. Chen, C. Wang, Y. Li, T. Zhang, Z. Chen, A. P. Pisano, L. Zhang, Q. Zhou, S. Xu, Monitoring of the central blood pressure waveform via a conformal ultrasonic device. *Nat. Biomed. Eng.* **2**, 687–695 (2018).
14. C. Wang, B. Qi, M. Lin, Z. Zhang, M. Makihata, B. Liu, S. Zhou, Y. H. Huang, H. Hu, Y. Gu, Y. Chen, Y. Lei, T. Lee, S. Chien, K. I. Jang, E. B. Kistler, S. Xu, Continuous monitoring of deep-tissue haemodynamics with stretchable ultrasonic phased arrays. *Nat. Biomed. Eng.* **5**, 749–758 (2021).
15. F. Wang, P. Jin, Y. Feng, J. Fu, P. Wang, X. Liu, Y. Zhang, Y. Ma, Y. Yang, A. Yang, X. Feng, Flexible Doppler ultrasound device for the monitoring of blood flow velocity. *Sci. Adv.* **7**, eabi9283 (2021).
16. M. Z. Nasrabadi, H. Tabibi, M. Salmani, M. Torkashvand, E. Zarepour, A comprehensive survey on non-invasive wearable bladder volume monitoring systems. *Med. Biol. Eng. Comput.* **59**, 1373–1402 (2021).
17. X. Xue, B. Zhang, S. Moon, G. X. Xu, C. C. Huang, N. Sharma, X. Jiang, Development of a wearable ultrasound transducer for sensing muscle activities in assistive robotics applications. *Biosensors* **13**, 134 (2023).
18. C.-C. Yu, A. Shah, N. Amiri, C. Marcus, M. O. G. Nayeem, A. K. Bhayadia, A. Karami, C. Dagdeviren, A conformable ultrasound patch for cavitation-enhanced transdermal cosmeceutical delivery. *Adv. Mater.* **35**, e2300066 (2023).
19. C. Wang, X. Chen, L. Wang, M. Makihata, H. C. Liu, T. Zhou, X. Zhao, Bioadhesive ultrasound for long-term continuous imaging of diverse organs. *Science* **377**, 517–523 (2022).

20. Y. Luo, M. R. Abidian, J. H. Ahn, D. Akinwande, A. M. Andrews, M. Antonietti, Z. Bao, M. Berggren, C. A. Berkey, C. J. Bettinger, J. Chen, P. Chen, W. Cheng, X. Cheng, S. J. Choi, A. Chortos, C. Dagdeviren, R. H. Dauskardt, C. A. di, M. D. Dickey, X. Duan, A. Facchetti, Z. Fan, Y. Fang, J. Feng, X. Feng, H. Gao, W. Gao, X. Gong, C. F. Guo, X. Guo, M. C. Hartel, Z. He, J. S. Ho, Y. Hu, Q. Huang, Y. Huang, F. Huo, M. M. Hussain, A. Javey, U. Jeong, C. Jiang, X. Jiang, J. Kang, D. Karnaushenko, A. Khademhosseini, D. H. Kim, I. D. Kim, D. Kireev, L. Kong, C. Lee, N. E. Lee, P. S. Lee, T. W. Lee, F. Li, J. Li, C. Liang, C. T. Lim, Y. Lin, D. J. Lipomi, J. Liu, K. Liu, N. Liu, R. Liu, Y. Liu, Y. Liu, Z. Liu, Z. Liu, X. J. Loh, N. Lu, Z. Lv, S. Magdassi, G. G. Malliaras, N. Matsuhisa, A. Nathan, S. Niu, J. Pan, C. Pang, Q. Pei, H. Peng, D. Qi, H. Ren, J. A. Rogers, A. Rowe, O. G. Schmidt, T. Sekitani, D. G. Seo, G. Shen, X. Sheng, Q. Shi, T. Someya, Y. Song, E. Stavrinidou, M. Su, X. Sun, K. Takei, X. M. Tao, B. C. K. Tee, A. V. Y. Thean, T. Q. Trung, C. Wan, H. Wang, J. Wang, M. Wang, S. Wang, T. Wang, Z. L. Wang, P. S. Weiss, H. Wen, S. Xu, T. Xu, H. Yan, X. Yan, H. Yang, L. Yang, S. Yang, L. Yin, C. Yu, G. Yu, J. Yu, S. H. Yu, X. Yu, E. Zamburg, H. Zhang, X. Zhang, X. Zhang, X. Zhang, Y. Zhang, Y. Zhang, S. Zhao, X. Zhao, Y. Zheng, Y. Q. Zheng, Z. Zheng, T. Zhou, B. Zhu, M. Zhu, R. Zhu, Y. Zhu, Y. Zhu, G. Zou, X. Chen, Technology roadmap for flexible sensors. *ACS Nano* **17**, 5211–5295 (2023).
21. S. Zhang, F. Li, High performance ferroelectric relaxor-$PbTiO_3$ single crystals: Status and perspective. *J. Appl. Phys.* **111**, 031301 (2012).
22. X. Gao, J. Yang, J. Wu, X. Xin, Z. Li, X. Yuan, X. Shen, S. Dong, Piezoelectric actuators and motors: Materials, designs, and applications. *Adv. Mater. Technol.* **5**, 1900716 (2020).
23. Q. Zhou, K. H. Lam, H. Zheng, W. Qiu, K. K. Shung, Piezoelectric single crystal ultrasonic transducers for biomedical applications. *Prog. Mater. Sci.* **66**, 87–111 (2014).
24. Z. Zhang, J. Xu, L. Yang, S. Liu, J. Xiao, X. Li, X.'. Wang, H. Luo, Design and comparison of PMN-PT single crystals and PZT ceramics based medical phased array ultrasonic transducer. *Sens. Actuators A Phys.* **283**, 273–281 (2018).
25. C.-M. Wong, Y. Chen, H. Luo, J. Dai, K. H. Lam, H. L. W. Chan, Development of a 20-MHz wide-bandwidth PMN-PT single crystal phased-array ultrasound transducer. *Ultrasonics* **73**, 181–186 (2017).
26. S. Trolier-McKinstry, S. Zhang, A. J. Bell, X. Tan, High-performance piezoelectric crystals, ceramics, and films. *Annu. Rev. Mat. Res.* **48**, 191–217 (2018).
27. F. Li, M. J. Cabral, B. Xu, Z. Cheng, E. C. Dickey, J. M. LeBeau, J. Wang, J. Luo, S. Taylor, W. Hackenberger, L. Bellaiche, Z. Xu, L. Q. Chen, T. R. Shrout, S. Zhang, Giant piezoelectricity of Sm-doped $Pb(Mg_{1/3}Nb_{2/3})O_3$-$PbTiO_3$ single crystals. *Science* **364**, 264–268 (2019).
28. Q. Li, Y. Liu, J. Liu, K. Song, H. Guo, F. Li, Z. Xu, Enhanced piezoelectric properties and improved property uniformity in Nd-doped PMN-PT relaxor ferroelectric single crystals. *Adv. Funct. Mater.* **32**, 2201719 (2022).
29. Y. Liu, Q. Li, L. Qiao, Z. Xu, F. Li, Achieving giant piezoelectricity and high property uniformity simultaneously in a relaxor ferroelectric crystal through rare-earth element doping. *Adv. Sci.* **9**, 2204631 (2022).
30. K. Kratkiewicz, A. Pattyn, N. Alijabbari, M. Mehrmohammadi, Ultrasound and photoacoustic imaging of breast cancer: Clinical systems, challenges, and future outlook. *J. Clin. Med.* **11**, 1165 (2022).
31. C.-Y. Lee, T.-L. Truong, P.-C. Li, Automated conformal ultrasound scanning for breast screening. *J. Med. Biol. Eng.* **38**, 116–128 (2018).
32. H. Kim, S. Lee, Characterization of electrical heating of graphene/PLA honeycomb structure composite manufactured by CFDM 3D printer. *Fash. Text.* **7**, 8 (2020).
33. B. Panda, M. Leite, B. B. Biswal, X. Niu, A. Garg, Experimental and numerical modelling of mechanical properties of 3D printed honeycomb structures. *Measurement* **116**, 495–506 (2018).
34. D. Lin, Z. Li, F. Li, Z. Xu, X. Yao, Characterization and piezoelectric thermal stability of PIN-PMN-PT ternary ceramics near the morphotropic phase boundary. *J. Alloys Compd.* **489**, 115–118 (2010).
35. H. J. Lee, S. Zhang, J. Luo, F. Li, T. R. Shrout, Thickness-dependent properties of relaxor-$PbTiO_3$ ferroelectrics for ultrasonic transducers. *Adv. Funct. Mater.* **20**, 3154–3162 (2010).
36. D. Lin, H. J. Lee, S. Zhang, F. Li, Z. Li, Z. Xu, T. R. Shrout, Influence of domain size on the scaling effects in $Pb(Mg_{1/3}Nb_{2/3})O_3$-$PbTiO_3$ ferroelectric crystals. *Scr. Mater.* **64**, 1149–1151 (2011).
37. C. Li, B. Xu, D. Lin, S. Zhang, L. Bellaiche, T. R. Shrout, F. Li, Atomic-scale origin of ultrahigh piezoelectricity in samarium-doped PMN-PT ceramics. *Phys. Rev. B* **101**, 140102 (2020).
38. S. Yan, Z. Sun, X. Chen, H. Qian, T. Zhao, H. Chen, L. Jiang, Growth and electrical properties of Yb^{3+} A-site doped PMNT:Yb single crystal. *J. Phys. Chem. Solid* **173**, 111103 (2023).
39. B. Jaffe, *Piezoelectric Ceramics* (Academic Press, 1971).
40. X. Yang, Z. Li, C. Fei, Y. Liu, D. Li, S. Hou, L. Zhang, F. Li, Y. Yang, Q. Zhou, Z. Xu, High frequency needle ultrasonic transducers based on Mn doped piezoelectric single crystal. *J. Alloys Compd.* **832**, 154951 (2020).
41. H.-T. Oh, H.-J. Joo, M.-C. Kim, H.-Y. Lee, Effect of Mn on dielectric and piezoelectric properties of 71PMN-29PT [$71Pb(Mg_{1/3}Nb_{2/3})O_3$-$29PbTiO_3$] single crystals and polycrystalline ceramics. *J. Korean Ceram. Soc.* **55**, 166–173 (2018).
42. K. Song, Q. Li, H. Guo, Q. Hu, Z. Li, F. Li, S. Fan, Z. Xu, Composition and electrical properties characterization of a 5'' diameter PIN-PMN-PT single crystal by the modified Bridgman method. *J. Alloys Compd.* **851**, 156145 (2021).
43. CTS Corporation, *The List of Piezoelectric Material Properties from CTS*; www.ctscorp.com/wp-content/uploads/CTS-Piezoelectric-Material-Properties_Full-List_July21.pdf.
44. W. Long, F. Guo, P. Fang, A. He, X. Li, Z. Xi, Temperature-dependent structure and electromechanical properties of Er doped PMN-PT single crystal grown by modified Bridgman technique. *J. Alloys Compd.* **902**, 163858 (2022).
45. K. K. Shung, *Diagnostic Ultrasound: Imaging and Blood Flow Measurements* (CRC Press, ed. 2, 2015).
46. W. R. Hedrick, D. L. Hykes, Beam steering and focusing with linear phiased arrays. *J. Diagn. Med. Sonogr.* **12**, 211–215 (1996).
47. A. H. Aitkenhead, J. A. Mills, A. J. Wilson, The design and characterization of an ultrasound phased array suitable for deep tissue hyperthermia. *Ultrasound Med. Biol.* **34**, 1793–1807 (2008).
48. A. Nowicki, Safety of ultrasonic examinations; thermal and mechanical indices. *Med. Ultrason.* **22**, 203 (2020).
49. M. Akram, M. Iqbal, M. Daniyal, A. U. Khan, Awareness and current knowledge of breast cancer. *Biol. Res.* **50**, 33 (2017).
50. M. S. Essa, M. H. Faheem, R. Abdalla, M. E. Zayed, The relationship between distance of breast cancer from the skin and incidence of axillary nodal metastasis in female patients with early cancer breast: Correlation between radiological and pathological distance. *Egypt. J. Surg.* **40**, 99–108 (2021).
51. C. V. Nguyen, R. F. Saraf, Tactile imaging of an imbedded palpable structure for breast cancer screening. *ACS Appl. Mater. Interfaces* **6**, 16368–16374 (2014).
52. M. Mance, K. Bulic, A. Antabak, M. Miloševic, The influence of size, depth and histologic characteristics of invasive ductal breast carcinoma on thermographic properties of the breast. *EXCLI J.* **18**, 549–557 (2019).
53. M. W. Mulholland, G. M. Doherty, G. R. Upchurch Jr., H. Alam, T. M. Pawlik, *Greenfield's Surgery: Scientific Principles & Practice* (Philadelphia Wolters Klewer, 2017).
54. V. Y. Sohn, Z. M. Arthurs, J. A. Sebesta, T. A. Brown, Primary tumor location impacts breast cancer survival. *Am. J. Surg.* **195**, 641–644 (2008).
55. G. Cserni, E. Chmielik, B. Cserni, T. Tot, The new TNM-based staging of breast cancer. *Virchows Arch.* **472**, 697–703 (2018).
56. J. DePolo, Breast cancer stages, 19 November 2022; www.breastcancer.org/pathology-report/breast-cancer-stages.
57. American Cancer Society, Understanding a breast cancer diagnosis; www.cancer.org/cancer/types/breast-cancer/understanding-a-breast-cancer-diagnosis.html.
58. M. Cianfrocca, L. J. Goldstein, Prognostic and predictive factors in early-stage breast cancer. *Oncologist* **9**, 606–616 (2004).
59. S. Łukasiewicz, M. Czeczelewski, A. Forma, J. Baj, R. Sitarz, A. Stanisławek, Breast cancer—Epidemiology, risk factors, classification, prognostic markers, and current treatment strategies—An updated review. *Cancer* **13**, 4287 (2021).
60. Z. S. Lima, M. R. Ebadi, G. Amjad, L. Younesi, Application of imaging technologies in breast cancer detection: A review article. *Open Access Maced. J. Med. Sci.* **7**, 838–848 (2019).
61. C. K. Kuhl, S. Schrading, C. C. Leutner, N. Morakkabati-Spitz, E. Wardelmann, R. Fimmers, W. Kuhn, H. H. Schild, Mammography, breast ultrasound, and magnetic resonance imaging for surveillance of women at high familial risk for breast cancer. *J. Clin. Oncol.* **23**, 8469–8476 (2005).
62. T. M. Kolb, J. Lichy, J. H. Newhouse, Comparison of the performance of screening mammography, physical examination, and breast US and evaluation of factors that influence them: An analysis of 27,825 patient evaluations. *Radiology* **225**, 165–175 (2002).
63. H. J. Shin, H. H. Kim, J. H. Cha, Current status of automated breast ultrasonography. *Ultrasonography* **34**, 165–172 (2015).
64. M. Zanotel, I. Bednarova, V. Londero, A. Linda, M. Lorenzon, R. Girometti, C. Zuiani, Automated breast ultrasound: Basic principles and emerging clinical applications. *Radiol. Med.* **123**, 1–12 (2018).
65. R. Rella, P. Belli, M. Giuliani, E. Bufi, G. Carlino, P. Rinaldi, R. Manfredi, Automated breast ultrasonography (ABUS) in the screening and diagnostic setting: Indications and practical use. *Acad. Radiol.* **25**, 1457–1470 (2018).
66. D. Lin, S. Zhang, E. Gorzkowski, S. Zhou, W. Liu, F. Li, Investigation of morphotropic phase boundaries in PIN-SN-PT relaxor ferroelectric ternary systems with high $T_{r\text{-}t}$ and T_c phase transition temperatures. *J. Eur. Ceram. Soc.* **37**, 2813–2823 (2017).
67. IEEE, *176-1987 - Standard on Piezoelectricity* (IEEE, 1988).
68. M. Kim, J. Kim, W. Cao, Aspect ratio dependence of electromechanical coupling coefficient of piezoelectric resonators. *Appl. Phys. Lett.* **87**, 132901 (2005).
69. GE ML6-15-D Ultrasound Transducer, AME Ultrasounds, https://ameultrasounds.com/products/ge-ml6-15-d-linear-array-probe.

70. Piezo material properties data sheet, Piezo.com, https://info.piezo.com/hubfs/Data-Sheets/piezo-material-properties-data-sheet-20201112.pdf.

Acknowledgments: C.D. thanks her late aunt, F. Caliskanoglu, who lost her life because of breast cancer in 2015, for inspiring this work since then. We thank T. Urman, C. Ricciardi, and X. Zhang, from MIT CCTR, and T. Langmead from GE Healthcare for assisting on the clinical study. We thank C. Barry, F. Lombardozzi, M. Keohane, and N. Hu from MIT COUHES for reviewing the IRB documents. We also thank laboratory members M. O. G. Nayeem and J.-H. Kim for constructive feedback on the manuscript preparation. **Funding:** This work was supported by NSF CAREER: Conformable Piezoelectrics for Soft Tissue Imaging (grant no. 2044688), 3M Non-Tenured Faculty Award, Sagol Weizmann-MIT Bridge Program, and MIT Media Lab Consortium funding. W.D. was supported by the NSF Graduate Research Fellowship Program under grant no. 2141064. Any opinions, findings, and conclusions or recommendations expressed in this material are those of the author(s) and do not necessarily reflect the views of the National Science Foundation. Human trials conducted at the MIT CCTR were supported in part by the National Center for Advancing Translational Sciences, NIH, award number UL1TR002544. This work was performed in part at the Harvard University Center for Nanoscale Systems (CNS), a member of the National Nanotechnology Coordinated Infrastructure Network (NNCI), which is supported by the NSF under NSF award no. ECCS-2025158. **Author contributions:** C.D. conceived the research idea and directed all research activities. L.Z. and C.D. designed research methodology and aims. D.L. processed and characterized the piezoelectric crystals. D.L. and F.L. analyzed the performance of crystals. W.L. supervised the materials investigation. C.D., W.D. and L.Z. designed, fabricated, and characterized the phased array. C.M. operated the Vantage 256 system and conducted all image processing. C.D. conceived the patch structure idea. C.D. and E.S. designed and fabricated the patch. A.A. assisted with the patch preparation. I.I.S. assisted with the device characterization and conducted the thermal stability test. L.O. assisted with the imaging scripts and IRB documents. W.D., C.M., and L.Z. conducted the imaging on phantoms. C.D. and W.D. executed the in vivo study. T.O. assisted on recruiting the subject and analyzing the images obtained by the cUSBr-patch. S.F. and D.S. assisted with manuscript preparation. W.D. and E.S. composed the layout of the supplementary movies and formed the movies. All authors contributed to manuscript writing. **Competing interests:** C.D. and L.Z. are inventors on a patent titled "Methods and apparatus for imaging with conformable ultrasound patch" (U.S. patent application no. 16/658,237, 23 April 2020). A.P.C. is on the Board of Analog Devices. The authors declare that they have no other competing interests. **Data and materials availability:** All data needed to evaluate the conclusions in the paper are present in the paper and/or the Supplementary Materials.

Submitted 9 March 2023
Accepted 26 June 2023
Published 28 July 2023
10.1126/sciadv.adh5325

ScienceAdvances

Conformable ultrasound breast patch for deep tissue scanning and imaging

Wenya Du, Lin Zhang, Emma Suh, Dabin Lin, Colin Marcus, Lara Ozkan, Avani Ahuja, Sara Fernandez, Ikra Iftekhar Shuvo, David Sadat, Weiguo Liu, Fei Li, Anantha P. Chandrakasan, Tolga Ozmen, and Canan Dagdeviren

Sci. Adv., **9** (30), eadh5325.
DOI: 10.1126/sciadv.adh5325